Growth, Properties, and Applications of Pulsed Laser Deposited Nanolaminate Ti₃AlC₂ Thin Films

Abhijit Biswas,[1] Arundhati Sengupta,[1] Umashankar Rajput,[1] Sachin Kumar Singh,[1] Vivek Antad,[2]
Sk Mujaffar Hossain,[1] Swati Parmar,[1,3] Dibyata Rout,[1] Aparna Deshpande,[1] Sunil Nair,[1] and
Satishchandra Ogale[1,4,*]

[1]*Department of Physics and Centre for Energy Science, Indian Institute of Science Education and Research
(IISER), Pune, Maharashtra 411008, India*
[2]*Department of Physics, Nowrosjee Wadia College, Pune, Maharashtra 411001, India*
[3]*Department of Technology, Savitribai Phule Pune University, Pune, Maharashtra 411007, India*
[4]*Research Institute for Sustainable Energy (RISE), TCG Centres for Research and Education in Science and
Technology (TCG-CREST), Kolkata 700091, India*

Recently, nanolaminated ternary carbides have attracted immense interest due to the concomitant presence of both ceramic and metallic properties. Here, we grow nanolaminate Ti₃AlC₂ thin films by pulsed laser deposition on *c*-axis-oriented sapphire substrates and, surprisingly, the films are found to be highly oriented along the (103) axis normal to the film plane, rather than the (000*l*) orientation. Multiple characterization techniques are employed to explore the structural and chemical quality of these films, the electrical and optical properties, and the device functionalities. The 80-nm thick Ti₃AlC₂ film is highly conducting at room temperature, with a resistivity of about 50 $\mu\Omega$ cm and a very-low-temperature coefficient of resistivity. The ultrathin (2 nm) Ti₃AlC₂ film has fairly good optical transparency (∼70%) and high conductivity (sheet resistance ∼735 Ω/sq) at room temperature. Scanning tunneling microscopy reveals the metallic characteristics (finite density of states at the Fermi level) at room temperature. The metal-semiconductor junction of the *p*-type Ti₃AlC₂ film and *n*-Si show the expected rectification (diode) characteristics, in contrast to the ohmic contact behavior in the case of Ti₃AlC₂/*p*-Si. A triboelectric-nanogenerator-based touch-sensing device, comprising of the Ti₃AlC₂ film, shows a very impressive peak-to-peak open-circuit output voltage (∼80 V). These observations reveal that pulsed laser deposited Ti₃AlC₂ thin films have excellent potential for applications in multiple domains, such as bottom electrodes, resistors for high-precision measurements, Schottky diodes, ohmic contacts, fairly transparent ultrathin conductors, and next-generation biomechanical touch sensors for energy harvesting.

I. INTRODUCTION

Nanolaminate ternary carbides and nitrides are a unique class of materials due to the concurrent existence of both ceramic and metallic properties therein; this is an unusually interesting combination of application-worthy functionalities [1–4]. These ternary materials are popularly known as *MAX* phases, ($M_{n+1}AX_n$, *n* = 1, 2, and 3; *M* is an early transition metal; *A* is mostly group IIIA and IVA elements; and *X* is C or N). More than 150 *MAX*-phase compounds have been discovered, all showing exceptional properties [5].

Among these ternary carbides and nitrides, Ti₃AlC₂ is one of the most studied compounds [6]. Structurally, it has a layered hexagonal symmetry, with lattice parameters

$a = 3.0753$ Å and $c = 18.578$ Å and space group P6₃/*mmc* [7]. The structure can be envisioned as the alternation of two edge-shared octahedral layers of Ti₆C (strong covalent bonding) separated by a two-dimensional (2D) closed packed layer of Al (metallic bonding). It is endowed with excellent thermal and chemical resistance, like that in ceramics, and good electrical and thermal conductivity. The electrical resistivity of bulk polycrystalline Ti₃AlC₂ is about 40 $\mu\Omega$ cm at room temperature, the temperature coefficient of resistivity (TCR) is small and, as expected, its electronic transport is anisotropic [8–10]. It also shows an unusual combination of properties, e.g., unusual softness (Vickers hardness ∼4 GPa), elastic stiffness, chemical robustness, and high damage tolerance at room temperature [1–4]. The discovery of *MX*ene (e.g., Ti₃C₂) derived from *MAX* (e.g., Ti₃AlC₂), a 2D analogue of graphene, has generated tremendous excitement about 2D functional

---

*satishogale@gmail.com; satish.ogale@tcgcrest.org

carbides and nitrides and their unique functionalities [11–13].

Extensive efforts have been expended by different groups to explore the possibility of obtaining high-quality films of different *MAX* phases (not limited only to the Ti_3AlC_2 phase) [3,14–16]. Pshyk *et al.* reported growth of the Ti_2AlC phase by electron-beam physical vapor deposition and studied the nanomechanical and microscale tribological properties [17]. Su *et al.* deposited pure-phase polycrystalline Ti_2AlC and Ti_3AlC thin films by reactive radiofrequency magnetron sputtering [18]. Rosén *et al.* grew epitaxial Ti_2AlC films through the high-current pulsed cathodic arc method [19]. Frodelius *et al.* studied the phase stability and initial low-temperature oxidation effect in Ti_2AlC thin films grown by the magnetic sputtering method [20,21]. Feng *et al.* also used magnetron sputtering to grow the Ti_2AlC-phase films [22]. Magnuson *et al.* investigated the electronic structure of dc magnetron sputtered Ti_3XC_2 ($X = Al$, Si, and Ge) films by soft x-ray emission spectroscopy [23]. Mauchamp *et al.* grew epitaxial ($000l$) Ti_2AlC phase thin films by dc magnetron sputtering and showed the anisotropic nature of electron transport [24]. Scabarozi *et al.* and Emmerlich *et al.* showed that magnetron-sputtered thin films of *MAX*-phase Ti_3SiC_2, Ti_4SiC_3, Ti_3GeC_2, Ti_2GeC, and Ti_2SnC were relatively good conductors [25,26]. There have also been reports on the growth of undoped and doped Cr_2GeC thin films by magnetron sputtering and the anisotropic nature of their electron transport, which is mediated through electron-phonon coupling [27,28]. For more exhaustive reports in the literature, one might look at the in-depth reviews by Eklund *et al.* [3,14], especially from the point of view of *MAX* thin films. Surprisingly, in spite of their unique physical properties, there are very few reports on the growth of Ti_3AlC_2 thin films of the right (312) phase and investigations into their various functional properties [13,29,30].

The majority of the thin-film growth of Ti_3AlC_2 has been performed either by chemical vapor deposition (CVD) or by the dc magnetron sputtering method [13,29, 30]. In all cases, a thin TiC seed layer is used to realize better and more uniform film growth. In terms of thin-film growth, the technique of pulsed laser deposition (PLD), which is employed herein, offers some distinct advantages over the CVD or sputtering methods, especially with regard to accurate stoichiometry transfer from a single target and high film density, leading to epitaxy (depending on substrate-film lattice parameter compatibility) due to enhanced adsorbate surface mobility endowed by high-energy radicals in the laser-generated plasma plume [31]. As stated by Eklund *et al.*, all of these processes (CVD, sputtering, cathodic arc deposition) have their own limitations that sets out the demand for other growth methods for not only Ti_3AlC_2 deposition, but also various other *MAX*-phase thin films [3,14]. However, we find only one report

on an attempt to grow Cr_2AlC *MAX*-phase thin films by PLD, indicating vast compositional deviation from the Cr_2AlC phase [32]. Therefore, we set out to examine the growth, properties, and application worthiness of thin films of a widely explored *MAX* phase, Ti_3AlC_2, using PLD. Given the high standing of the PLD and laser molecular beam epitaxy (MBE) techniques in the field of oxide heteroepitaxy, oxide electronics, and spintronics, we feel that success in using the PLD method for growth of high-quality films of *MAX* phases could translate into exciting device property regimes through integration with oxide films.

Among the goals of this work, one goal is to go down to the ultrathin limit of thickness and explore the occurrence of some potentially emergent phenomena in such ultrathin films. We indeed find that high-quality Ti_3AlC_2 thin films [remarkably with high orientation along (103)] can be obtained by PLD, and these films are not only highly conducting at room temperature (thus, useful as bottom electrodes for numerous layered functional materials), but also have a very low temperature coefficient of resistivity (useful for high-precision measurements). The ultrathin (2 nm) films show fairly high ($\sim$70%) optical transparency and good electrical conductivity (sheet resistance $\sim$735 Ω/sq), making them useful as moderate transparent conductors for some optoelectronic applications. Moreover, these p-type Ti_3AlC_2 films also render impressive rectifying characteristics with n-Si and ohmic contact with p-Si. They also exhibit impressive triboelectric sensing device performance, which is useful for biomechanical energy harvesting.

II. EXPERIMENTAL METHODS

The Ti_3AlC_2 films are grown by PLD (KrF laser of wavelength 248 nm, pulse width 20 ns). The Ti_3AlC_2 target is synthesized by ball-milling a mixture of Ti, Al, and TiC powders (1:1.5:2 molar ratio) at 100 rpm for 24 h under an Ar atmosphere, and then heating the mixture in a covered alumina crucible in a furnace at 1400 °C for 2 h under an Ar atmosphere, as per standard protocols [33]. The polycrystalline single-phase Ti_3AlC_2 product [as confirmed by x-ray diffraction (XRD), see Fig. S1 within the Supplemental Material [34]], as obtained from the furnace, is in the form of a hard solid, which is then polished and used as a target. For deposition, we use c-Al_2O_3 (0001) sapphire, n- or p-Si (001), and flexible Kapton substrates, depending on the application and characterization goal. Prior to deposition, atomically flat surfaces of c-Al_2O_3 substrates are prepared by annealing at 1000 °C for 1 h. Films on c-Al_2O_3 and Si are grown by using the following growth conditions: growth temperature about 700 °C, laser fluence about 3 J/cm^2, target to substrate distance about 40 mm, and repetition rate of 10 Hz. All films are grown under vacuum ($\sim$10^{-6} mbar). For fabrication of the

nanogenerator device, we also use flexible Kapton substrates and grow the films at 400 °C, by keeping all other growth conditions identical.

XRD is performed with a Bruker D2 Phaser x-ray diffractometer. Atomic force microscopy (AFM) is used for surface topography analysis and measuring the thickness of the films, using a Nanosurf AFM instrument (Switzerland). Raman spectra are recorded with a 2.33 eV (~532 nm) excitation energy laser. X-ray photoelectron spectroscopy (XPS) is performed with a K-Alpha x-ray photoelectron spectrometer (Thermo-Fisher Scientific Instrument, UK). It is carried out in an ultrahigh vacuum chamber (2×10^{-9} mbar) by using an Al $K\alpha$ x-ray source with 6 mA beam current (beam spot size on the sample is ~400 μm). Before recording XPS, in situ ion-beam etching (energy 1000 eV) is used for 30 s to remove surface contamination.

Electrical measurements are performed using the standard ac transport four-probe method by using a Quantum Design physical property measurement system (PPMS), within the temperature range of $T = 5$–300 K. For magnetoresistance measurements, the magnetic field is applied along the out-of-plane direction.

Scanning tunneling microscopy (STM) is performed using Omicron ultrahigh vacuum (UHV) at room temperature, with a pressure of 10^{-8} mbar. Before imaging, films are in situ annealed for 60 min in three cycles for 20 min each at 150 °C. The images are processed using image analysis software (SPIP 6.0.9, Image Metrology, Denmark). A tungsten (W) tip is used for imaging. The parameters used for imaging are as follows: bias voltage $V = 2$ V, set-point current $I = 100$ pA (for 2 nm film); $V = 1$ V and $I = 100$ pA (for 80 nm film).

I-V characteristics of Ti_3AlC_2 films grown on n- and p-type Si (001) substrates are measured using a Keithley 4200 semiconductor characterization system (SCS) connected to a standard probe station (Semiprobe, USA). Depending on the position of the W probe on the devices, two modes are defined (forward bias and reverse bias). All I-V measurements are carried out in the current perpendicular to the plane (CPP) mode, with a voltage sweep of ± 3 V and voltage steps of 0.05 V at $T = 300$ K.

Triboelectric nanogenerator (TENG) devices are fabricated using Ti_3AlC_2 films. A contact-mode TENG architecture is adopted for the design of the touch sensor. To maintain the gap between the top and bottom layers, four pieces of 3M double-sided tape (1 mm thick) are also used and are attached at the edges. The total active device area is 1.5×1.5 cm^2. The electrical outputs are measured using a Keithley DMM7510 multimeter by soldering copper wires on the copper tapes on both electrodes (Al and Ti_3AlC_2), with a short-circuit current of 3 μA. We use the PASCO force sensor to measure the applied force from a human arm, which is about 15 N.

III. RESULTS AND DISCUSSION

A. Structural characterization

The XRD patterns shown in Fig. 1(a) indicate the presence of only two film peaks, in addition to the (000l) substrate peaks corresponding to the c-axis sapphire. We had expected that the (000l) orientation of the substrate would translate into the film and, as such, we look for the same in the XRD patterns. However, in this case, one must see multiple peaks corresponding to (000l) ($l = 2$, 4, 6, etc.), starting from (0002) $2\theta \approx 9.44°$. However, surprisingly, we find only two peaks near (0008) and (00016) and no other peaks. Thus, it becomes clear that the film does not grow along the nominally expected (000l) orientation. Interestingly, the XRD peaks for the (103) and (206) planes of Ti_3AlC_2 are also quite close to the same two 2θ values, where clear but somewhat broader peaks are seen in Fig. 1(b). The leads us to conclude that the film grows in the form of a high degree of orientation along the (103) orientation normal to the film plane.

The interesting choice of (103) orientation by the growing film in the PLD process can be partly elucidated by a comparison of possible surface terminations of the Ti_3AlC_2 lattice surface along the (000l) and (103) orientations and is possibly related to an interface chemistry scenario. Towards this end, we present in Fig. 1(c) the surface atomic arrangements in the cases of the two orientations with top and side views. It is clear that, in the case of the (000l) orientation, the surface terminations are in the form of the Ti, Al, or C planes, while the terminations for the (103) orientation are mixed-atom terminations. In the single Ti_3AlC_2 target-based PLD process, all atoms from the target (Ti, Al, C) and corresponding radicals impinge on the hot (700 °C) substrate at the same time. The atoms (with energy in the range of 0.1 eV to several electronvolts for the pulsed laser generated plasma) undergo physisorption and surface diffusion followed by chemisorption or incorporation into the growth front. Initially, clusters form and they grow laterally and vertically, as driven by the in-plane and out-of-plane step diffusion rates that are coguided by the growth temperature and the chemistry of bonding on the surface and at the step edges. Since the top of the c-axis-oriented sapphire substrate would basically have a fully oxygenated surface, the surface oxygen atoms would strive to bond with the impinging Ti, Al, and C atoms and the corresponding single-atom or multiatom compound radicals. Since the Ti, Al, and C atoms arrive in a nominal proportion of about 3:1:2, the chances of forming initial Ti-C related local clusters with a scattered presence of low-density Al atoms are higher than the formation of facile stoichiometric Ti, Al, and C clusters. Although a detailed analysis will have to follow complex Monte Carlo growth simulation, in the absence of it, one could argue that the above scenario does not quite favor the formation of successive ordered layers of

Ti, Al, and C that will have to form for the film to acquire (000*l*) orientation. It would need selective upward (and downward) step diffusion of one species over the other, which could be kinetically more complicated, rather than a scenario wherein all three atom types are available in the same plane and rearrange themselves laterally more than vertically. Given the fact that the lattice symmetry and parameters for the two plane orientations [as shown in Fig. 1(c)] are quite similar to the sapphire top surface for *c*-axis orientation, it appears that the film chooses the (103) orientation, at least under the growth conditions used in this work. Importantly, as shown later in the same section, the film stoichiometry does faithfully follow the target stoichiometry, as is known for the PLD process, namely, the Ti:Al:C ratio is 3:1:2. Moreover, no other secondary XRD peaks are seen to suggest multiple phases. Thus, the (103) oriented growth of Ti_3AlC_2 is strongly indicated.

The forgoing arguments do not mean that there could not be another PLD parameter space that could lead to the (000*l*) film orientation. One clue to the nontriviality in this respect appears from the broad nature of the (103) and (206) peaks, which suggest the presence of some interface diffusion and reaction, leading to a tilted angle distribution of grain orientation. The most appropriate strategy under this condition would possibly be the introduction

of a diffusion barrier layer, such as the TiC (111) layer, which is insightfully employed in some works on (000*l*) oriented film growth [13,29,30]. Indeed, it has been suggested that such a layer minimizes the high in-plane strain and improves wetting [13,29,30]. We will continue to pursue work on different barrier layers in further studies, because the corresponding parameters for the all-PLD process will have to be differently optimized, compared with other techniques such, as sputtering.

The surface topography revealed by AFM mimics a clear step-terrace pattern of the substrate for ultrathin films. Indeed, all films have atomically smooth surfaces with a surface roughness of less than 1 nm [inset of Fig. 1(a) and Fig. S2 within the Supplemental Material [34]].

We also examine the elemental ratio of the Ti_3AlC_2 film (deliberately grown on Si to avoid inseparable contribution of Al from the Al_2O_3 substrate) by field-emission scanning electron microscopy (FESEM) energy-dispersive x-ray spectroscopy (EDAX) analysis, which shows that the Ti:Al ratio is close to about 3:1 (35.7:11.3), as expected [Fig. S3(a) within the Supplemental Material [34]]. This confirms the faithful stoichiometry transfer by the PLD process, which is its hallmark. Furthermore, to verify the formation of the hexagonal Ti_3AlC_2 phase, we deposit Ti_3AlC_2 directly on the carbon-coated Cu grid by PLD (at
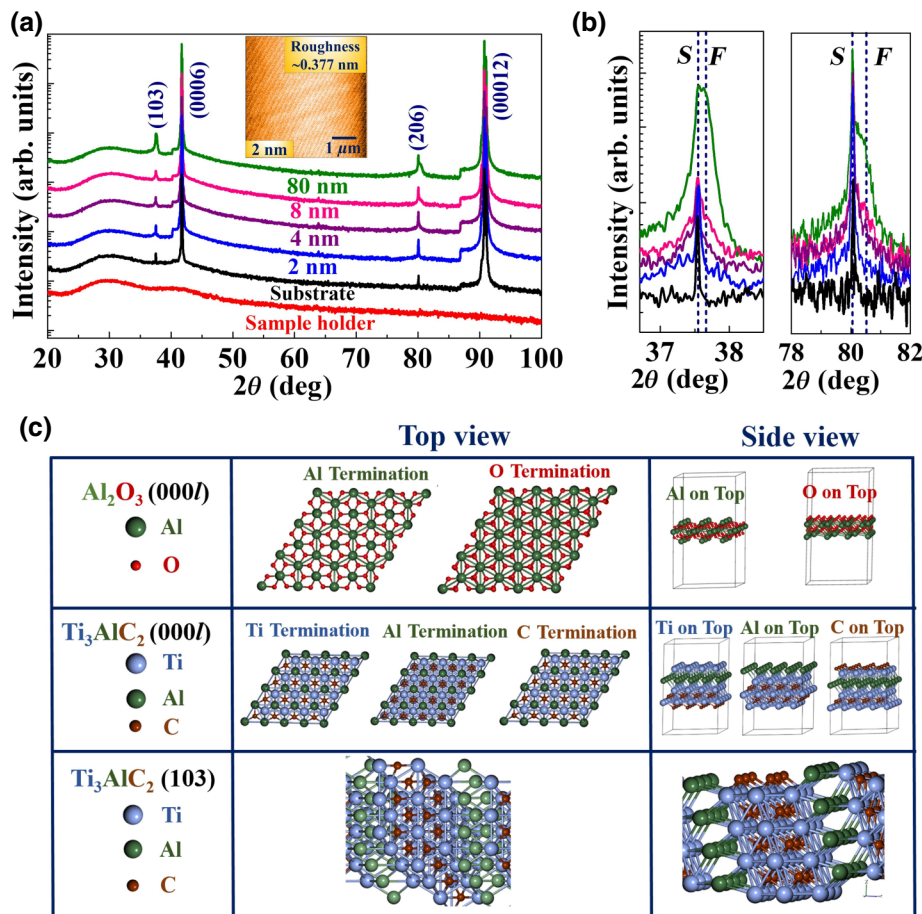

FIG. 1. (a) X-ray diffraction pattern of Ti_3AlC_2 thin films of various thicknesses grown on c-Al_2O_3 (0001) substrates (broad humps at lower angle are due to the sample holder, as shown). Inset shows a topographic image obtained by atomic force microscopy of a Ti_3AlC_2 film (2 nm), showing an atomically smooth surface with a clear step-terrace structure and roughness of 0.377 nm. (b) In XRD, separate contributions emanating from substrate (*S*) and film (*F*) are clearly visible. (c) Schematic of Al_2O_3 (000*l*) and Ti_3AlC_2 along (000*l*) and (103) planes, as top views and side views. These structures are drawn using VESTA software.

room temperature) and record the top-view high-resolution transmission electron microscopy (HRTEM) image. This can give us some indication of the initial stage of thin-film growth. From the image, we can clearly see the local formation of the hexagonal lattice structure [Fig. S3(b) within the Supplemental Material [34], Fig. 1(c)]. EDAX once again confirms that the elemental ratio of Ti:Al is about 3:1 (76.1:23.9); this further confirms that the film grown by PLD is hexagonal Ti_3AlC_2.

To gain further insights into the microstructural and bonding aspects, we record room-temperature Raman spectra for the case of the bulk 80 nm film. For the Ti_3AlC_2 phase, based on symmetry considerations, ideally we should see seven Raman-active modes $(2A_{1g} + 2E_{1g} + 3E_{2g})$ [35], where A_{1g} and E_{1g} correspond to the out-of-plane vibrations, and E_{2g} corresponds to the in-plane vibration. However, literature reports have shown that only six modes are visible in the spectra [36], which we clearly see for our film as well [Fig. 2(a)]. It is to be noted, however, that the main peak in the range of 600–700 cm^{-1} is considerably broadened [36], possibly suggesting multiple contributions (such as intrinsic inhomogeneity related to the chemical compositions, grain size, and morphology), as well as a degree of expected strain gradient (distribution) in the film. We show the fitting of the broad signature with multiple contributions [inset of Fig. 2(a)]. Two of these (A_{1g} and E_{2g}) correspond to the pure Ti_3AlC_2 phase [36], albeit with a small strain-induced shift. The other smaller contributions emanate from the surface oxide, which is known to be in the form of Ti_2CO_2

[11], and possibly small contributions from the sapphire substrate. Additionally, we also observe a Raman signature around 400 cm^{-1} (peak indicated by an asterisk), as reported by Presser *et al.* [36], associated possibly with a degree of disorder. These data reflect that the Ti_3AlC_2 film has a thin layer of surface oxide because of the known high reactivity of the surface.

We also perform XPS on the in situ mildly sputter-cleaned 80 nm Ti_3AlC_2 film. The XPS data for the Ti 2*p*, Al 2*p*, and C 1*s* are shown in Figs. 2(b)–2(d). Peak fitting is performed using CasaXPS software. As noted by other groups, the Ti 2*p* XPS data for the as-grown film (Fig. S4 within the Supplemental Material [34]) show multiple peaks due to surface oxidation [37]. The C 1*s* XPS results for as-received films also show the presence of carboxylate (-COO) surface groups [13]. Notably, after in situ cleaning, the spectrum changes drastically, especially for Ti 2*p* and C 1*s*. The Ti 2*p* spectrum can be best fitted with three pairs (for $2p_{1/2}$ and $2p_{3/2}$) of curves, with a universal spin-orbit peak splitting of about 6 eV [Fig. 2(b)]. These three pairs can be assigned to Ti-Al-C, Ti(IV) oxide, and Ti(III) oxide, respectively. The spectrum matches quite well with the reported data of CVD-grown Ti_3AlC_2 thin film [13].

Interestingly, in the case of Al 2*p*, we can see only the higher binding energy peak of Al oxide [Fig. 2(c)] and do not observe the expected metallic Ti-Al peak at about 72 eV. We believe that the high reactivity of Ti_3AlC_2 causes oxidation of the top few layers, where the major XPS signal emanates from, and therefore, the feature is either small or negligible. The absence of the Ti-Al peak
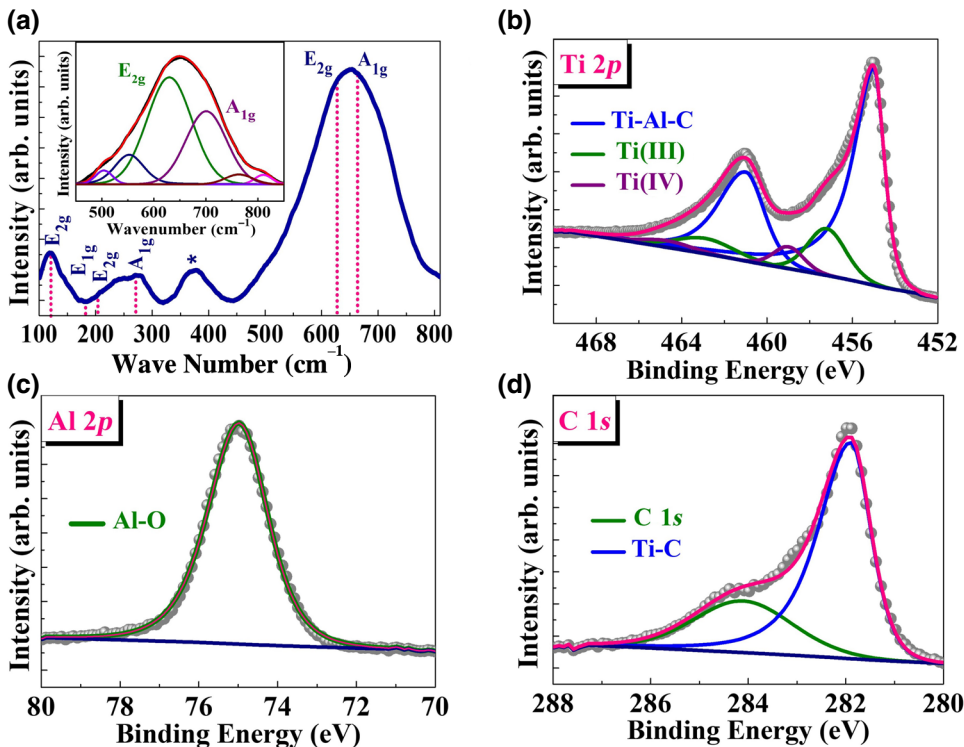

FIG. 2. (a) Raman spectrum and (b)-(d) X-ray photoelectron spectra of in situ surface-cleaned 80 nm Ti_3AlC_2 film. Asterisk in the Raman spectrum corresponds to possible disorder and a substrate-related peak.

is also reported for the ceramic Mo_2TiAlC_2 sample [38]. In our case, wherein deposition is performed directly on sapphire without a nucleating (or barrier) layer of TiC, as done in several other papers [13,29], the high substrate-induced strain leads to film growth by three-dimensional island or grain growth mode (as also confirmed by AFM), rather than a layer-by-layer mode. Thus, in addition to bulk diffusion, the columnar morphology will cause grain boundary oxygen diffusion, leading to higher degree of oxidation of the top few layers. Eklund *et al.* have clearly stated that, when growing a film of Al_2O_3 at high temperature, Al and O migrate from the substrate and, at the film-substrate interface, substrate species also form along with the deposited species [14]. Interestingly, we find that the Al $2p$ spectrum does show the expected about 72 eV contribution from Ti-Al, when the film is grown at a much lower growth temperature of 400 °C (Fig. S5 within the Supplemental Material [34]). This implies that oxidation most possibly occurs during growth at high temperature due to residual oxygen present in the system.

For the C $1s$ core, the peak at a low binding energy corresponds to Ti-C [Fig. 2(d)] [13,37]. In addition, importantly, the contribution from the Ti-C bond is enhanced significantly after in situ cleaning of the surface [Fig. 2(d) and Fig. S4 within the Supplemental Material [34]], as reflected by the absence of carboxylate (-COO) surface groups.

B. Carrier transport

Electrical measurements on the 80-nm thick Ti_3AlC_2 film show a resistivity (ρ) of about $50\,\mu\Omega$ cm at $T = 300$ K [Fig. 3(a)], comparable to the bulk polycrystalline Ti_3AlC_2 phase ($\sim 40\,\mu\Omega$ cm at $T = 300$ K) [8–10,39]. This low ρ at $T = 300$ K is quite remarkable and is a consequence of the presence of substantial density of states (DOS) at the Fermi level dominated by the d-d orbitals of Ti [7]. Interestingly, in our Ti_3AlC_2 films, the derivative of resistivity ($d\rho/dT$) is very weakly dependent on T [inset of Fig. 3(a)] with a resistivity value of $\rho \sim 62\,\mu\Omega$ cm, even at $T = 5$ K. The TCR (defined as $\alpha = 1/\rho_T(d\rho/dT)$, ρ_T at a given temperature) is about 4.5×10^{-4} K^{-1} (~ 360 ppm/°C) within a temperature range of $150 \leq T \leq 200$ K; these are characteristics of a bad metal, where quasiparticle states collapse due to strong inelastic scattering [40].

Hall Effect measurements at $T = 300$ K show (data not included here) that charge carriers are of p type (holes are the majority carriers) with a typical metal-like carrier concentration (n_p) of about 10^{28}/m^3 and mobility (μ) of about 7.5×10^{-4} m^2 V^{-1} s^{-1}, which are comparable to the observed values for bulk polycrystalline Ti_3AlC_2 [8]. Magnetoresistance (MR), defined as $\Delta\rho/\rho_0 = [\rho(B) - \rho(0)]/\rho(0)$, is noted to be positive with a quadratic magnetic field dependence (MR $\propto B^2$) [Fig. 3(b)], as is usually observed in a typical metal, as a consequence of the

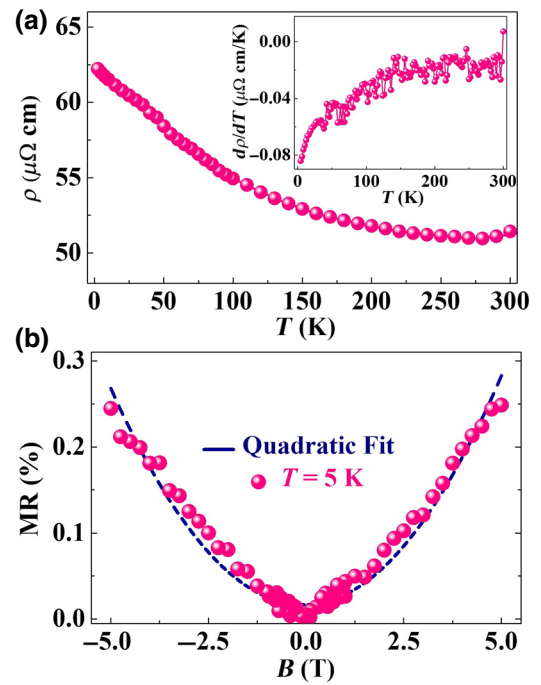FIG. 3. Temperature-dependent carrier transport of 80 nm Ti_3AlC_2 film grown on c-Al_2O_3 (0001) substrate. (a) Resistivity shows highly conducting nature at room temperature, with very small variation in resistivity over the whole temperature range (inset). (b) Positive quadratic-field-dependent magnetoresistance, showing normal metal-like behavior.

Lorentz contribution. All of these analyses indicate that, at room temperature, our PLD-grown layered Ti_3AlC_2 thin film is highly conducting with holes (p type) as majority charge carriers, and electronically it lies on the boundary between a metal and semiconductor.

We further examined the thickness-dependent sheet resistance (R_S) and optical transmission by examining films from 80 nm thick down to ultrathin 2 nm, since ultrathin films can potentially generate interesting emergent phenomena, as a consequence of quantum confinement, high surface to volume ratio, surface states and charges, and interfacial strain. Upon reducing the film thickness, the R_S is observed to increase (Fig. 4 and Fig. S6 within the Supplemental Material [34]) due to a reduction in band filling and an increase in effective disorder, as the disorder becomes more effective in the scattering of charge carriers in thinner films. Surface and interface scattering contributions, as well as grain boundary scattering contributions, are known to be accentuated with a reduction in film thickness below a certain value commensurate with the mean free path [41]. Interestingly, even the ultrathin 2 nm film shows an impressive and application-worthy conductivity ($R_S \sim 735\,\Omega$/sq) at $T = 300$ K. Equally important, the TCR is very low (as the dR_S/dT is very low in Fig. S7 within the Supplemental Material [34]), confirming
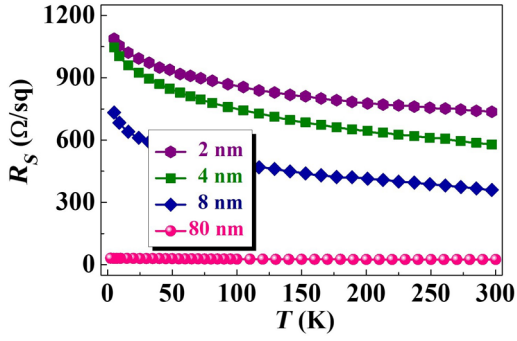
FIG. 4.   Thickness-dependent sheet resistance (R_S) of Ti_3AlC_2 thin films grown on c-Al_2O_3 (0001) substrates.

TABLE I.   Transparency and room-temperature sheet resistance (R_S) of Ti_3AlC_2 films grown on c-Al_2O_3 (0001) substrates.

Film	Thickness (nm)	Transparency (%)	R_S (Ω/sq)
Ti_3AlC_2	2	$\sim$70	$\sim$735
	4	$\sim$55	$\sim$580
	8	$\sim$30	$\sim$360
	80	$\sim$8	$\sim$20

that the basic material character of being on the metal-semiconductor boundary and its properties are retained even in few-unit-cell ultrathin films.

Understanding the nature of electronic transport in Ti_3AlC_2 phases is quite tricky, as revealed by several interesting past studies. Barsoum *et al.* reported on the temperature dependence of resistivity of polycrystalline samples of two (312) (Ti_3AlC_2, Ti_3SiC_2) and one (413) (Ti_4AlN_3) *MAX* phases over the wide temperature regime and interpreted (compared) data in terms of the charge carrier concentrations and defect scattering contributions [8]. They argued that the conductivity was lower in Ti_3AlC_2 due to dearth of carriers. A detailed analysis by Finkel *et al.* [9], again on polycrystalline Ti_3AlC_2, emphasized the need to invoke a two-band framework to explain transport for the case of Ti_3AlC_2 and suggested that carrier concentrations remained almost constant over a broad temperature range, while mobility changed due to phonon scattering and neutral impurities. Reports on Ti_2AlC and Cr_2GeC thin films suggest that electron-phonon interactions also play an important role in electron transport [24,27]. Notably, the room-temperature resistivity of the Ti_3AlC_2 film (grown by magnetron sputtering) reported in the literature is about 40–50 $\mu\Omega$ cm [8,9,29], which is similar to our PLD-grown films.

In our case, for the 80 nm film, except for a small drop in resistivity with decreasing temperature over the $270 \leq T \leq 300$ K range, the resistivity is seen to increase very slightly with decreasing temperature. Although the room-temperature resistivity of our film is very close to the reported value, it shows a mild increase in resistivity while decreasing the temperature; this trend is the opposite of that for normal metal-like characteristics. Notably, the rise in resistivity with lowering of temperature is not very rapid, as expected for a semiconductor. This can happen if the film has a lateral grainlike structure (even though it is oriented) and the grain boundary transport competes with intragrain metallic transport. Therefore, one can argue that the observed behavior is a consequence of the competition

between intergrain transport (at the grain boundaries) and delocalized intragrain metal-like transport.

The grain boundary aspects in polycrystalline samples and their possible contributions to transport have also not yet been fully addressed. Therefore, one can argue that possibly moderate strain gradient disorder or density of point defects, due to possible slight off-stoichiometry, could cause localization effects, rendering a mild upturn of the resistivity. Since the suggested two-band model envisages the active role of both carrier types, preferential localization of one over the other can affect the overall majority-minority carrier concentration And their respective mobilities. Interestingly, the MR observed in our case at $T = 5$K is not only positive, but has the value of the quadratic coefficient $\alpha = 1.03 \times 10^{-2}$ m^4/V^2s^2 (MR $= \alpha \times B^2$), which is much higher than that of the reported value of about 10^{-4} m^4/V^2s^2 at $T = 5$K [9]. A low concentration of defects or disorder can result in hopping behavior, and this can be influenced by the magnetic field, leading to the noted positive MR.

C. Optical transmission

Interestingly, while the bulk 80 nm film is expectedly black due to high conductivity, the ultrathin (2 nm) film is fairly transparent ($\sim$70%) in the visible range, in spite of its high conductivity. As expected, the transparency decreases systematically with the increase of the film thickness [Fig. 5(a) and Fig. S8 within the Supplemental Material [34]). In our case, we note that the 4 nm Ti_3AlC_2 film is about 55% transparent, whereas the 8 nm film is about 30% transparent and the 80 nm one is black [Fig. 5(b) and Table I]. Considering the highly conducting nature of Ti_3AlC_2 films with their ceramic-type robustness (high scratch resistance), they could possibly be used in some applications in the place of wide-band-gap semiconductor films (e.g., tin-doped indium oxide) [42].

D. STM

We also perform in situ STM for both the ultrathin ($\sim$2 nm) and thicker Ti_3AlC_2 ($\sim$80 nm) films at $T = 300$ K to elucidate the density of electronic states. STM evaluation on Ti_3AlC_2-phase thin films has not yet been performed. STM topographical images of the in situ annealed 2 and 80 nm Ti_3AlC_2 films are shown in Figs. 6(a) and 6(b), respectively. To gain an insight into the nature of the
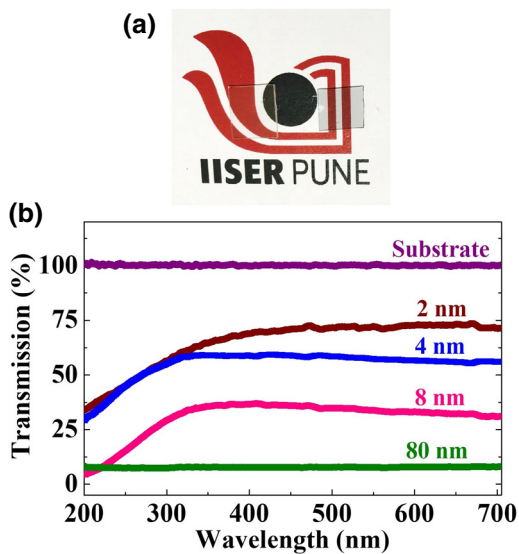
FIG. 5. (a) Transparency of both-sides-polished bare c-Al_2O_3 (0001) substrate (left) and deposited 2 nm Ti_3AlC_2 ultrathin film (right). (b) Thickness-dependent optical transmission in the visible wavelength range, showing that the ultrathin 2 nm film transmits about 70% of the light, with a sheet resistance of about 735 Ω/sq at room temperature.
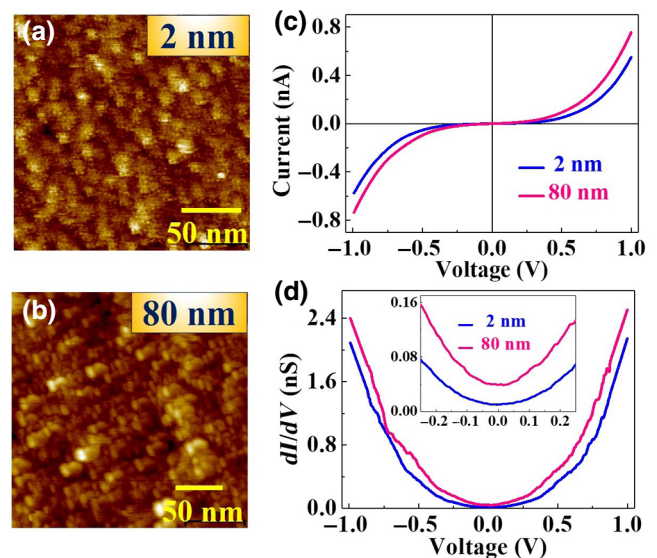

FIG. 6. (a), (b) In situ STM topographic images, and (c) current versus voltage and (d) differential conductance (dI/dV) spectra of 2 and 80 nm Ti_3AlC_2 films taken at room temperature within the applied bias voltage range of ± 1 V.

density of electronic states, we also measure the *I-V* characteristics. Numerical differentiation of *I-V* curves yields dI/dV spectra, which are a measure of the local DOS.

The STM dI/dV data for the as-grown sample exposed to air and measured under ambient conditions show specific features that are typical of localized states, which can be attributed to the surface groups (Fig. S9 within the Supplemental Material [34]). However, for the in situ annealed films (and subsequent STM images recorded inside the UHV chamber), we note a parabolic-type (not strictly parabolic) nature of differential conductance with a finite DOS at the Fermi level (E_F), signifying metallicity for the in situ annealed films [Figs. 6(c) and 6(d)]. Interestingly, around E_F, the nature of this dependence resembles the calculated DOS reported by Zhou *et al.*, which mainly originates from the nearly free-electron state of Ti $3d$ [7]. It may be noted that, although the electronic structure calculations about this material are interesting, the experimental work is lacking, with subsequent fabrication and evaluation of device functionalities. Our work is a step in this direction, since the PLD process gives immense control over the surface quality and subsequent properties of the films and their in situ heterostructures (known well in the field of oxides).

E. Schottky diodes

Considering the highly conducting yet robust ceramic nature of Ti_3AlC_2 (unlike noble metals, such as Au and Ag, which are mechanically soft with issues of thermal stability

and high-current-induced material transport in the form of electromigration), we examine the electrical (*I-V*) characteristics of the heterojunction between the p-Ti_3AlC_2 film and n-Si (semiconductor) substrate, which is a Schottky diode configuration. An ultrathin layer of surface oxide, as revealed by XPS, in principle, may qualify it more as a p-i-n tunnel junction, rather than a pure p-n junction. The p-Ti_3AlC_2/n-Si junction exhibits a clear rectifying character [Fig. 7(a)], which is consistent with the p-type charge carriers of Ti_3AlC_2 discussed earlier in Sec. III B. Significantly, the low forward junction potential reveals the typical nature expected for a Schottky junction. The forward to reverse current ratio at 0.5 V (-0.5 V) is 21.3, while at 1 V (-1 V) it is 36.6. In contrast, for the p-Ti_3AlC_2/p-Si junction, we observe a non-Schottky behavior in the *I-V* characteristics [Fig. 7(b)], as both layers are of p type, but with a degree of nonlinearity. Recently, Fashandi *et al.* have shown the formation of ohmic contacts for various (312) *MAX* phases grown on SiC with remarkable stability, even after 1000 h of ageing at 600 °C in air [43]. Moreover, rapid thermal annealing (900 °C for 4 min) of Ti_3SiC_2 also results in the formation of ohmic contacts [44]. We also anneal the p-Ti_3AlC_2/p-Si film (in situ annealing inside the PLD chamber at 700 °C for 3 h following deposition) to check whether the *I-V* characteristics become fully ohmic or not. Interestingly, the *I-V* curve shows enhanced linearity (Fig. S10 within the Supplemental Material [34]) with the formation of an almost ohmic contact (within the depicted small range of applied voltage) for Ti_3AlC_2/p-Si [inset of Fig. 7(b)]. Transport across the Schottky contact (p-n junction) can be viewed within the framework
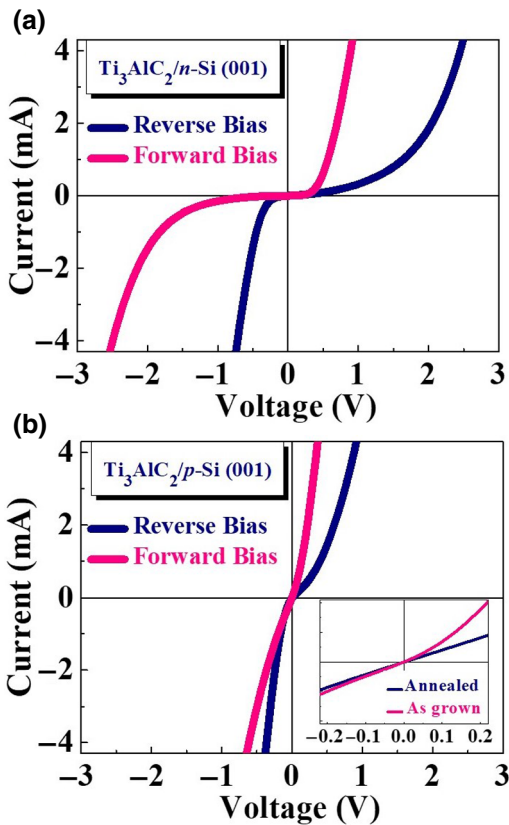
FIG. 7. (a) Room temperature *I-V* characteristics of 80 nm Ti_3AlC_2 film grown on *n*-Si (001) substrate, showing rectification behavior. (b) In contrast, almost ohmiclike contact is observed for film grown on *p*-Si (001). After in situ annealing at 700 °C for 3 h, over the small bias voltage range, full ohmic contact is observed for p-Ti_3AlC_2/p-Si, over the small bias range (inset).

of the thermionic emission theory, diffusion theory, or the effect of both, depending upon the specific theoretical models [45]. Since these are related to mobility, specifically high mobility (in the case of thermionic emission) and low mobility (in the case of diffusion), we conjecture that diffusion across the interface is mostly applicable in our case, as Ti_3AlC_2 shows rather low mobility at $T = 300$ K ($\mu \sim 10^{-4}$ m^2 V^{-1} s^{-1}). This metal-semiconductor junction feature can be attributed to Fermi level (E_F) pinning by the electronic midgap states or the interface defect states, as nanoscale inhomogeneity is ubiquitous at the interface of thin-film heterostructures [45].

F. TENG

Finally, having confirmed the highly metallic nature with *p*-type charge carriers of Ti_3AlC_2 films, we proceed to explore the efficacy of these films as an electron-accepting electrode in the TENG application. In general, TENG devices are in high demand for sensing, tribotronics, or mechanical energy-harvesting applications [46,47].
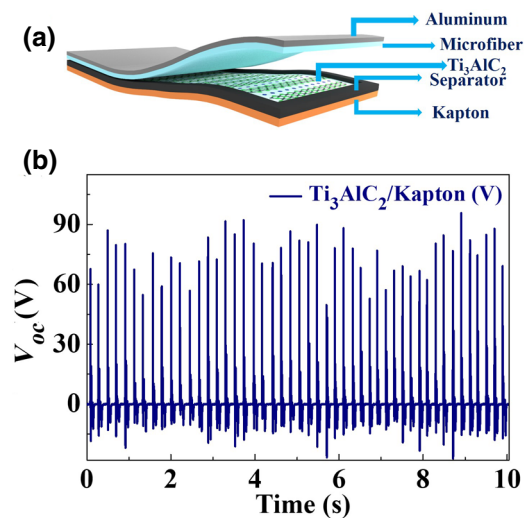

FIG. 8. (a) Schematic of a TENG device containing Ti_3AlC_2 film grown on flexible Kapton substrate. (b) Open-circuit voltage (V_{oc}) of the TENG-based touch-sensing device.

Indeed, energy harvesting from human movements for portable and wearable electronic devices receives considerable attention these days. However, the materials currently in use are limited to a few polymeric systems (including some wherein active materials are embedded in polymers, thereby forming composites), wherein issues of efficient charge transport and transfer, as well as bond cleavage, wear, and physical transfer of the material are matters of continuing concern [48]. Recently, several interesting designs of TENGs, including the use of 2D materials and biomaterials, have been researched with very impressive outcomes [49]. Since *MX*ene has laterally slidable layers with a low out-of-plane conductivity [12], we conjecture that even thin films of the robust Ti_3AlC_2 phase, with excellent mechanical stability and high conductivity, could render interesting TENG effects. Thus, we fabricate and test TENG devices by using Ti_3AlC_2 films grown on flexible Kapton substrate, which enables homologous interface contact between the actuator and the device. This also suits the TENG requirement to adapt to flexible and wearable devices.

The schematic of a typical TENG device is shown in Fig. 8(a), where *p*-type conducting Ti_3AlC_2 is used as part of a touch-sensor device. As stated above, Ti_3AlC_2 not only provides positive charges (*p* type), but also acts as a highly conducting bottom electrode for contact. In contrast, glass microfiber filter paper is used to supply negative charge carriers. On the top, aluminum is used as a top electrode. Functionally, when both layers are almost in contact with each other (by pressing), both *p*- and *n*-type carriers feel dipolar forces and exchange of carriers takes place at the interface, generating triboelectric surface charges at the interface. When the pressure is released,

the charges (both +ve and –ve) move away from each other. However, to compensate for the interfacial triboelectric effect, they build up opposite charges on the bottom surface (of Ti_3AlC_2) and top surface (of aluminum), generating a potential difference. Our TENG device shows an impressive peak-to-peak open-circuit output voltage (V_{oc}) of about 80 V [Fig. 8(b)], which can be attributed to efficient contact electrification that can be enhanced by the interface texture of Ti_3AlC_2 grown on Kapton.

IV. CONCLUSIONS

Nanolaminate Ti_3AlC_2 thin films are grown by the PLD technique (which is better known in the fields of metals oxides and oxide electronics-spintronics). The films show accurate transfer of the stoichiometry from the target to the film, which is a hallmark of the single-target PLD technique. Remarkably, the films are noted to grow with (103) orientation normal to the film plane. These films exhibit various interesting application-worthy physical properties, especially high conductivity with low TCR, even down to very low temperature. They are fairly transparent in ultra-thin form, yet retaining very high conductivity at room temperature. Furthermore, STM is employed to characterize the Ti_3AlC_2 films, which show metallic characteristics at room temperature. The PLD-grown Ti_3AlC_2 also shows rectification (diode) characteristics (p-n junction) with n-Si and ohmic-like contact (p-p junction) with p-Si. The films also show a remarkable TENG-based biomechanical touch-sensing capability. The ability to grow high-quality *MAX*-phase thin films by PLD can open up interesting avenues for their integration with functional metal oxides to generate the next generation of interesting devices [50].

ACKNOWLEDGMENTS

[1] M. Radovic and M. W. Barsoum, MAX phases: Bridging the gap between metals and ceramics, Am. Ceram. Soc. Bull. **92**, 20 (2013).

[2] M. W. Barsoum, The $M_{N+1}AX_N$ phases: A New class of solids, Prog. Solid State Chem. **28**, 201 (2000).

[3] P. Eklund, M. Beckers, U. Jansson, H. Högberg, and L. Hultman, The $M_{n+1}AX_n$ phases: Materials science and thin-film processing, Thin Solid Films **518**, 1851 (2010).

[4] M. W. Barsoum and M. Radovic, Elastic and mechanical properties of the MAX phases, Annu. Rev. Mater. Res. **41**, 195 (2011).

[5] M. Sokol, V. Natu, S. Kota, and M. W. Barsoum, On the chemical diversity of the MAX phases, Trends Chem. **1**, 210 (2019).

[6] N. V. Tzenov and M. W. Barsoum, Synthesis and characterization of Ti_3AlC_2, J. Am. Ceram. Soc. **83**, 825 (2000).

[7] Y. C. Zhou, X. H. Wang, Z. M. Sun, and S. Q. Chen, Electronic and structural properties of the layered ternary carbide Ti_3AlC_2, J. Mater. Chem. **11**, 2335 (2001).

[8] M. W. Barsoum, H–I Yoo, I. K. Polushina, V. Yu. Rud, Yu. V. Rud, and T. El-Raghy, Electrical conductivity, thermopower, and hall effect of Ti_3AlC_2, Ti_4AlN_3 and Ti_3SiC_2, Phys. Rev. B **62**, 10194 (2000).

[9] P. Finkel, M. W. Barsoum, J. D. Hettinger, S. E. Lofland, and H. I. Yoo, Low-temperature transport properties of nanolaminate Ti_3AlC_2 and Ti_4AlN_3, Phys. Rev. B **67**, 235108 (2003).

[10] G. Ya Khadzhai, R. V. Vovk, T. A. Prichna, E. S. Geovorkyan, M. V. Kislitsa, and A. L. Solovjov, Electrical and thermal conductivity of the Ti_3AlC_2 MAX phase at low temperatures, Low Temp. Phys. **44**, 451 (2018).

[11] M. Naguib, M. Kurtoglu, V. Presser, J. Lu, J. Niu, M. Heon, L. Hultman, Y. Gogotsi, and M. W. Barsoum, Two-Dimensional nanocrystals produced by exfoliation of Ti_3AlC_2, Adv. Mater. **23**, 4248 (2011).

[12] M. Naguib, V. N. Mochalin, M. W. Barsoum, and Y. Gogotsi, 25th anniversary article: Mxenes: A New family of Two-diemnsional materials, Avd. Mater. **26**, 992 (2014).

[13] J. Halim, M. R. Lukatskaya, K. M. Cook, J. Lu, C. R. Smith, L. Näslund, S. J. May, L. Hultman, Y. Gogotsi, P. Eklund, and M. W. Barsoum, Transparent conductive Two-dimensional titanium carbide epitaxial thin films, Chem. Mater. **26**, 2374 (2014).

[14] P. Eklund, J. Rosén, and POÅ Persson, Layered ternary $M_{n+1}AX_n$ phases and their 2D derivative MXene: An overview from a thin-film perspective, J. Phys. D: Appl. Phys. **50**, 113001 (2017).

[15] M. Magnuson and M. Mattesini, Chemical bonding and electronic-structure in MAX phases as viewed by X-ray spectroscopy and density functional theory, Thin Solid Films **621**, 108 (2017).

[16] A. S. Ingason, A. Petruhins, and J. Rosén, Towards structural optimization of MAX phases as epitaxial thin films, Mater. Res. Lett. **4**, 152 (2016).

[17] A. V. Pshyk, E. Coy, M. Kempiński, B. Scheibe, and S. Jurga, Low-temperature growth of epitaxial Ti_2AlC MAX phase thin films by low-rate layer-by-layer PVD, Mater. Res. Lett. **7**, 244 (2019).

[18] R. Su, H. Zhang, D. J. O'Connor, L. Shi, X. Meng, and H. Zhang, Deposition and characterization of Ti_2AlC MAX phase and Ti_3AlC thin films by magnetron sputtering, Mater. Lett. **179**, 194 (2016).

[19] J. Rosén, L. Ryves, POÅ Persson, and M. M. M. Bilek, Deposition of epitaxial Ti$_2$AlC thin films by pulsed cathodic arc, J. App. Phys. **101**, 056101 (2007).

[20] J. Frodelius, J. Lu, J. Jensen, D. Paul, L. Hultman, and P. Ekund, Phase stability and initial low-temperature oxidation mechanism of Ti$_2$AlC thin films, J. Eur. Ceram. Soc. **33**, 375 (2013).

[21] J. Frodelius, P. Eklund, M. Beckers, POÅ Persson, H. Högberg, and L. Hultman, Sputter deposition from a Ti$_2$AlC target: Process characterization and conditions for growth of Ti$_2$AlC, Thin Solid Films **518**, 1621 (2010).

[22] Z. Feng, P. Ke, and A. Wang, Preparation of Ti$_2$AlC MAX phase coating by DC magnetron sputtering deposition and vacuum heat treatment, J. Mater. Sci. Technol. **31**, 1193 (2015).

[23] M. Magnuson, J.-P. Palmquist, M. Mattesini, S. Li, R. Ahuja, O. Eriksson, J. Emmerlich, O. Wilhelmsson, P. Eklund, H. Högberg, L. Hultman, and U. Jansson, Electronic structure investigation of Ti$_3$AlC$_2$, Ti$_3$SiC$_2$, and Ti$_3$GeC$_2$ by soft x-ray emission spectroscopy, Phys. Rev B **72**, 245101 (2005).

[24] V. Mauchamp, W. Yu, L. Gence, L. Piraux, T. Cabioc'h, V. Gauthier, P. Eklund, and S. Dubois, Anisotropy of the resistivity and charge-carrier sign in nanolaminated Ti$_2$AlC: Experiment and ab initio calculations, Phys. Rev. B **87**, 235105 (2013).

[25] T. H. Scabarozi, P. Eklund, J. Emmerlich, H. Högberg, T. Meehan, P. Finkel, M. W. Barsoum, J. D. Hettinger, L. Hultman, and S. E. Lofland, Weak electronic anisotropy in the layered nanolaminate T$_2$GeC, Solid State Commun. **64**, 498 (2008).

[26] J. Emmerlich, P. Eklund, D. Rittrich, H. Högberg, and L. Hultman, Electrical resistivity of Ti$_{n+1}$AC$_n$ (A = Si, Ge, Sn, n = 1–3) thin films, J. Mater. Res. **22**, 2279 (2007).

[27] P. Eklund, M. Bugnet, V. Mauchamp, S. Dubois, C. Tromas, J. Jensen, L. Piraux, L. Gence, M. Jaouen, and T. Cabioc'h, Epitaxial growth and electrical transport properties of Cr$_2$GeC thin films, Phys. Rev. B **84**, 075424 (2011).

[28] T. H. Scabarozi, S. Benjamin, B. Adamson, J. Applegate, J. Roche, E. Pfeiffer, C. Steinmetz, C. Lunk, M. W. Barsoum, J. D. Hettingera, and S. E. Lofland, Combinatorial investigation of the stoichiometry, electronic transport and elastic properties of (Cr$_{1-x}$V$_x$)$_2$GeC thin films, Scr. Mater. **66**, 85 (2012).

[29] O. Wilhelmsson, J.-P. Palmquist, T. Nyberg, and U. Jansson, Deposition of Ti$_2$AlC and Ti$_3$AlC$_2$ epitaxial films by magnetron sputtering, Appl. Phys. Lett. **85**, 1066 (2004).

[30] O. Wilhelmsson, J.-P. Palmquist, E. Lewin, J. Emmerlich, P. Eklund, P. O. A. Persson, H. Hö gberg, S. Li, R. Ahuja, O. Eriksson, L. Hultman, and U. Jansson, Deposition and characterization of ternary thin films within the Ti-Al-C system by DC magnetron sputtering, J. Cryst. Growth **291**, 290 (2006).

[31] M. Opel, Spintronic oxides grown by laser-MBE, J. Phys. D: Appl. Phys. **45**, 033001 (2012).

[32] C. Lange, M. Hopfeld, M. Wilke, J. Schawohl, Th. Kups, M. W. Barsoum, and P. Schaaf, Pulsed laser deposition from a pre-synthesized Cr$_2$AlC MAX phase target with and without ion-beam assistance, Phys. Status Solidi A **209**, 545 (2012).

[33] M. Alhabeb, K. Maleski, B. Anasori, P. Lelyukh, L. Clark, S. Sin, and Y. Gogotsi, Guidelines for synthesis and processing of Two-dimensional titanium carbide (Ti$_3$C$_2$TxMXene), Chem. Mater. **29**, 7633 (2017).

[34] See the Supplemental Material at http://link.aps.org/supplemental/10.1103/PhysRevApplied.13.044075 for structural, morphological, electrical, optical, STM, and I-V characterizations.

[35] J. E. Spanier, S. Gupta, M. Amer, and M. W. Barsoum, Vibrational behavior of the M$_{n+1}$AX$_n$ phases from first-order Raman scattering (M = Ti, V, Cr, A = Si, X = C, N), Phys. Rev. B **71**, 012103 (2005).

[36] V. Presser, M. Naguib, L. Chaput, A. Togo, G. Hug, and M. W. Barsoum, First-order Raman scattering of the MAX phases: Ti$_2$AlN, Ti$_2$AlC$_{0.5}$N$_{0.5}$, Ti$_2$AlC, (Ti$_{0.5}$V$_{0.5}$)$_2$AlC, V$_2$AlC, Ti$_3$AlC$_2$, and Ti$_3$GeC$_2$, J. Raman Spectosc. **43**, 168 (2011).

[37] W. H. K. Ng, E. S. Gnanakumar, E. Batyrev, S. K. Sharma, P. Pujari, H. F. Greer, W. Zhou, R. Sakidja, G. Rothernberg, M. W. Barsoum, and N. R. Shiju, The Ti$_3$AlC$_2$ MAX phase as an efficient catalyst for oxidative dehydrogenation of n-butane, Angew. Chem. Int. Ed **57**, 1485 (2018).

[38] B. Anasori, M. Dahlqvist, J. Halim, E. J. Moon, J. Lu, B. C. Hosler, E. N. Caspi, S. J. May, L. Hultman, P. Eklund, J. Rosén, and M. W. Barsoum, Experimental and theoretical characterization of ordered MAX phases Mo$_2$TiAlC$_2$ and Mo$_2$Ti$_2$AlC$_3$, J. Appl. Phys. **118**, 094304 (2015).

[39] K. Goc, W. Prendota, L. Chlubny, T. Straczek, W. Tokarz, P. Bprpwaik (Chachlowska), K. Witulska (Chabior), M. M. Bućko, J. Przewoźnik, and J. Lis, Structure, morphology and electrical transport properties of the Ti$_3$AlC$_2$ materials, Ceram. Int. **44**, 18322 (2018).

[40] K. Takenaka, A. Ozawa, T. Shibayama, N. Kaneko, T. Oe, and C. Urano, Extremely low temperature coefficient of resistance in antiperovskite Mn$_3$Ag$_{1-x}$Cu$_x$N, Appl. Phys. Lett. **98**, 022103 (2011).

[41] J. M. Camacho and A. I. Oliva, Surface and grain boundary contributions in the electrical resistivity of metallic nanofilms, Thin Solid Films **515**, 1881 (2006).

[42] D. S. Ginley and C. Bright, Transparent conducting oxides, MRS Bull. **25**, 15 (2000).

[43] H. Fashandi, M. Dahlqvist, J. Lu, J. Palisaitis, S. I. Simak, I. A. Abrikosov, J. Rosén, L. Hultman, M. Andersson, A. L. Spetz, and P. Eklund, Synthesis of Ti$_3$AuC$_2$, Ti$_3$Au$_2$C$_2$ and Ti$_3$IrC$_2$ by nobel metal substitution reaction in Ti$_3$SiC$_2$ for high-temperature-stable ohmic contacts to SiC, Nat. Mater. **16**, 814 (2017).

[44] B. Pecz, L. Toth, M. A. di Forte-Poisson, and J. Vacas, Ti$_3$sic$_2$ formed in annealed Al/Ti contacts to p-type SiC, Appl. Surf. Sci. **206**, 8 (2003).

[45] W. Ramdan, S. B. Ogale, S. Dhar, L. F. Fu, S. R. Shinde, D. C. Kundaliya, M. S. R. Rao, N. D. Browning, and T. Venkatesan, Electrical properties of epitaxial junctions between Nb:SrTiO$_3$ and optimally doped, underdoped, and Zn-doped YBa$_2$Cu$_3$O$_{7-\delta}$, Phys. Rev. B **72**, 205333 (2005).

[46] F.-R. Fan, Z.-Q. Tian, and Z. L. Wang, Flexible triboelectric generator!, Nano Energy **1**, 328 (2012).

[47] C. Wu, A. C. Wang, W. Ding, H. Guo, and Z. L. Wang, Triboelectric nanogenerator: A foundation of the energy for the New Era, Avd. Eng. Mater. **9**, 1802906 (2019).

[48] A. Šutka, K. Malnieks, L. Lapčinskis, P. Kaufelde, A. Linarts, A. Berzina, R. Zabels, V. Jurkans, I. Gornves, J. Bloms, and M. Knite, The role of intermolecular forces in contact electrification on polymer surfaces and triboelectric nanogenerators, Energy Environ. Sci. **12**, 2417 (2019).

[49] M. Seol, S. Kim, Y. Cho, K.-E. Byun, H. Kim, J. Kim, S. K. Kim, S.-W. Kim, H.-J. Shin, and S. Park, Triboelectric series of 2D layered materials, Adv. Mater. **30**, 1801210 (2018).

[50] K. T. Kang, J. Park, D. Suh, and W. S. Choi, Synergetic behavior in 2D layered material/complex oxide heterostructures, Adv. Mater. **31**, 1803732 (2019).